Letters

Transient DC Bias and Universal Dynamic Modulation of Multiactive Bridge Converters

Shusheng Wei, Di Mou, *Member, IEEE*, Wusong Wen, Zhengming Zhao, *Fellow, IEEE*, and Kai Li, *Member, IEEE*

***Abstract*—Multiactive bridge (MAB) converters are attracting increasing attention due to their advantages of mutual electrical isolation and bidirectional power flow capability among different ports. However, the presence of transient dc bias in MAB can increase the current stress and lead to transformer saturation, thus affecting the system reliability. This letter establishes a quantitative and general description of the transient dc bias based on the instantaneous middle current of the high-frequency transformer and proposes a general dynamic modulation method to eliminate the bias, which is robust irrespective of the phase-shift modulation methods and the power flow directions. Also, it works at both the normal and startup modes. More importantly, the proposed method can ensure that the high-frequency transformer current reaches to new steady state without transient dc bias within one half cycle. Finally, the MAB experimental prototypes, including a triple active bridge and a modular MAB with a high-frequency ac bus, are built to verify the superior performance of the proposed method.**

***Index Terms*—Dynamic modulation, multiactive bridge (MAB), single phase shift (SPS), transient dc bias.**

I. Introduction

THE multiactive bridge (MAB) converter, as shown in Fig. 1, is becoming a hot topic in both academia and industry in recent years since it could take advantage of the magnetic coupling and provide multiports to integrate the multiple dc voltage domains in many applications, such as power electronic transformer, more electric aircraft or all-electric ship, and energy router for smart homes [1]–[4]. However, the presence of transient dc bias in MAB can increase current stress and lead to transformer saturation, which can affect the reliability of equipment operation.

Manuscript received March 11, 2022; revised April 22, 2022 and May 10, 2022; accepted May 11, 2022. Date of publication May 16, 2022; date of current version June 24, 2022. This work was supported by the National Nature Science Foundation of China under Grant U2034201. *(Corresponding author: Di Mou.)*

Shusheng Wei, Di Mou, Wusong Wen, and Zhengming Zhao are with the Department of Electrical Engineering, Tsinghua University, Beijing 100084, China (e-mail: weiss13@mails.tsinghua.edu.cn; dimou428@mail.tsinghua.edu.cn; wenwusong@163.com; zhaozm@tsinghua.edu.cn).

Kai Li is with the School of Electrical Engineering, Beijing Jiaotong University, Beijing 100044, China (e-mail: kaili@bjtu.edu.cn).

Color versions of one or more figures in this article are available at https://doi.org/10.1109/TPEL.2022.3175320.

Digital Object Identifier 10.1109/TPEL.2022.3175320

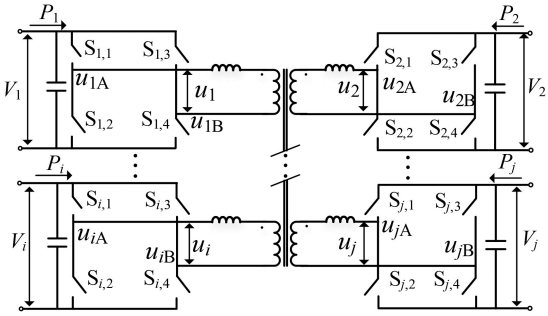

Fig. 1. Circuit of MAB converter.

Recently, the transient dc bias current due to the abrupt phase-shift change in the dual active bridge (DAB) and its variant structure has been studied in some pieces of literature [5]–[14]. In [6]–[8], based on the conventional single phase-shift (SPS) modulation scheme, an intermediate angle into the phase shift is introduced to eliminate the dc bias. In [9] and [10], the double-side SPS modulation schemes are proposed to mitigate the transient dc bias current, respectively. In [11] and [12], current-mode modulation schemes are proposed to realize the fast response without the transient dc bias, but the current sensor with high bandwidth is required. In [13] and [14], the valid control scheme for triple phase-shift modulation schemes is proposed. The voltage-second balance principle for each half-bridge is used to derive the elegant method in [13], where the transient bias of both the winding and the magnetizing currents is mitigated. However, the scenarios of different power flow should be considered. The derivation in [14] is quite complex by exhaustive method for several possible pulsewidth modulation (PWM) patterns. Also, the transient magnetizing current bias is not considered. In MAB, the power cross-coupling feature and the increasing number of the control variables make the transient dc bias much more complex than the traditional DAB converters, while the related research work is quite scarce. It is worth mentioning that when the phase-shift plus duty cycle modulation, which is also called the general phase-shift (GPS) modulation [4] instead of SPS, is utilized, the complexity is increased further.

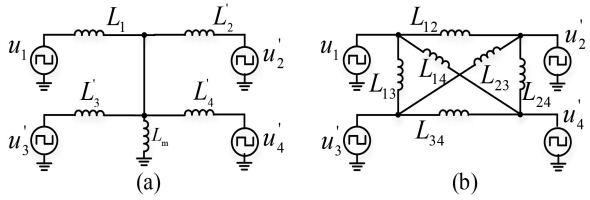

Fig. 2. Simplified equivalent model of MAB. (a) *Y* type. (b) Δ type.

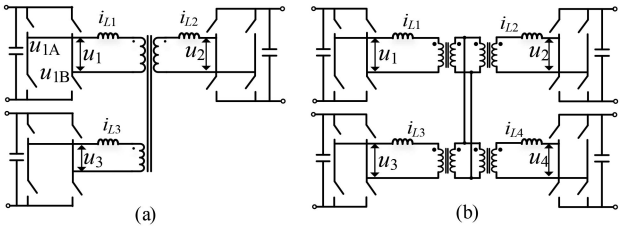

Fig. 3. MAB converters. (a) TAB converter. (b) MMAB converter.

To remove the transient dc bias, this letter introduces the general transient dc bias model for MAB based on the instantaneous middle current of the high-frequency transformer, which is irrespective of the power direction and modulation method. Then, a universal dynamic modulation method is proposed for transient dc bias mitigation. The method is independent of the modulation methods and valid for both the normal and startup modes without increasing the control frequency. Finally, the superior performance is verified by the experimental results of a triple active bridge (TAB) and a common high-frequency ac bus modular multiactive bridge (MMAB) converter.

II. MAB Converter and the Transient DC Bias

A. Basic Principle of MAB

The basic principle of MAB is illustrated below with a four-port MAB converter, where the simplified equivalent *Y* and Δtype circuits are shown in Fig. 2. In the circuit, L_i' is the phase-shift inductance of the branch *i* referred to the branch 1. L_m is the equivalent magnetizing inductor. u_i' is the ac voltage of the active bridge *i* referred to the branch 1. L_{ij} in the Δtype circuit, as shown in Fig. 2(b), represents the inductance between the branch *i* and *j*. N_i is the transformer turns of the windings *i*. The basic relationship is shown as follows:

$$u_i' = (N_1/N_i)u_i, \quad L_i' = (N_1/N_i)^2 L_i,$$
$$L_{ij} = L_i' L_j' \left(1/L_m + \sum_{l=1}^{n} 1/(L_l')\right). \tag{1}$$

Besides, in Fig. 1, $S_{i,1}$, $S_{i,2}$, $S_{i,3}$, and $S_{i,4}$ are the four switches and u_{iA} and u_{iB} are the output voltages of the half bridges in the branch *i*. V_i and P_i are the dc voltage and power, respectively. The transferred power among the different ports is coupled together, which is completely dependent on the phase-shift angle of each port.

Among the MAB structures, the typical ones are the TAB, as shown in Fig. 3(a), and MMAB with a common high-frequency ac bus [15], as shown in Fig. 3(b). For the MMAB converter, the multiwinding transformer is replaced by the independent two-winding transformers connected in parallel on the secondary side [16]–[18]. This structure replaces the common core in the MAB with a high-frequency ac bus, thus creating an intermediate energy convergence path among different ports. It is easy for modularity and scalability, which is beneficial when the power capacity of the converter is high.

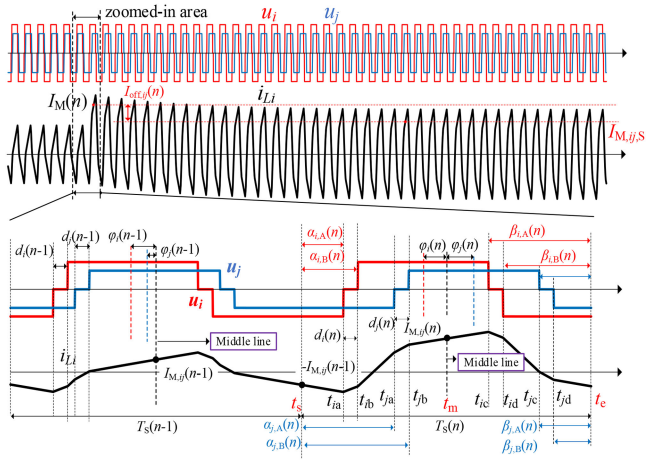

Fig. 4. Transient dc bias current in DAB consisting of the branch *i* and *j*.

B. Instantaneous Middle Current of the Windings in MAB

Actually, it is difficult to use the instantaneous currents at the switching point to represent the transient dc current bias as there are many switching moments due to the switching ON and OFF actions of other branches in one cycle. Therefore, the middle current I_M, which is instantaneous current at the middle line in a period, is used to define and calculate the transient dc bias current.

Considering the equivalent virtual DAB converter consisting of the branch *i* and *j* for generality, the voltage and current waveforms are shown in Fig. 4. $I_{M,ij}$ (*n*) is the middle current in the *n*th cycle. u_i and u_j are the ac voltages of bridge *i* and *j*, and φ_i and φ_j are the corresponding phase-shift angles. K_{ij} is the dc voltage ratio of the branch *i* and *j*. d_i and d_j are the inner phase-shift duties of branch *i* and *j*. The middle current $I_{M,ij}$ at steady state could be derived as (2), which shows that the middle current is only related to the phase-shift angles φ_i and φ_j

$$I_{M,ij} = V_i(\varphi_j - k_{ij}\varphi_i)/(2\pi f_S L_{ij} k_{ij}),$$
$$k_{ij} = V_i/((N_i/N_j)V_j). \tag{2}$$

C. Model of the Transient DC Bias Current

The transient dc bias current of the virtual DAB $I_{\mathrm{off},ij}$ is shown in Fig. 4. The t_s, t_m, and t_e are the start, half, and end moments of the *n*th cycle, respectively. T_S is the switching period and f_S is the switching frequency. At the moment t_s, the phase-shift angles and inner phase-shift duties change from $\varphi_i(n-1)$, $\varphi_j(n-1)$, $d_i(n-1)$, and $d_j(n-1)$ to $\varphi_i(n)$, $\varphi_j(n)$, $d_i(n)$, and $d_j(n)$, respectively. The time t_{ia}, t_{ib}, t_{ic}, and t_{id} are the switching

moments of u_i when u_i steps up from $-V_i$ to 0, 0 to V_i, V_i to 0, and 0 to $-V_i$, respectively. Similarly, t_{ja}, t_{jb}, t_{jc}, and t_{jd} are the switching moments for u_j. The transient dc bias current decays gradually to 0 after several cycles, while the middle current $I_{M,ij}$ reaches the steady-state value $I_{M,ij,S}(n)$ as follows:

$$I_{M,ij,S}(n) = V_i(\varphi_j(n) - k_{ij}\varphi_i(n))/(2\pi f_S L_{ij} k_{ij}). \quad (3)$$

The middle current in the nth cycle $I_{M,ij}(n)$ is calculated as

$$\begin{aligned} I_{M,ij}(n) &= i_L(t_s) + \Delta I_L = -I_{M,ij}(n-1) + \Delta I_L \\ &= -\frac{V_i(\varphi_j(n-1) - k_{ij}\varphi_i(n-1))}{2\pi f_S L_{ij} k_{ij}} + \Delta I_L \end{aligned} \quad (4)$$

where ΔI_L is the current ripple during 0 to $T_S/2$ and $I_L(t_s)$ is the initial current in the nth cycle. Defining the "rising duration" α and "falling duration" β as follows: $\alpha_{i,A}(n) = t_{ia}$–t_s, $\alpha_{i,B}(n) = t_{ib} - t_s$, $\beta_{i,A}(n) = t_e - t_{ic}$, and $\beta_{i,B}(n) = t_e - t_{id}$. The values of $\alpha_{i,A}(n)$ and $\alpha_{i,B}(n)$ for the conventional modulation method are as follows:

$$\begin{aligned} \alpha_{i,A}(n) &= (1 - d_i(n))\frac{T_S}{4} + \frac{\varphi_i(n)}{\pi}\frac{T_S}{2}, \\ \alpha_{i,B}(n) &= \alpha_{i,A}(n) + d_i(n)\frac{T_S}{2}. \end{aligned} \quad (5)$$

For brevity, ΔI_L can be calculated by adding up the two ripple currents due to u_i and u_j according to the superposition principle as

$$\begin{cases} \Delta I_L = \Delta I_{L,u_i} + \Delta I_{L,u_j} \\ \Delta I_{L,u_i} = \frac{-V_i}{L_{ij}} \cdot \alpha_{i,A}(n) + \frac{V_i}{L_{ij}} \cdot \left(\frac{T_S}{2} - \alpha_{i,B}(n)\right)\frac{T_S}{2} \\ \Delta I_{L,u_j} = \frac{V_i}{k_{ij}L_{ij}} \cdot \alpha_{j,A}(n) + \frac{-V_i}{k_{ij}L_{ij}} \cdot \left(\frac{T_S}{2} - \alpha_{j,B}(n)\right). \end{cases} \quad (6)$$

Combing (3)–(6), the dc bias current for the conventional modulation method is derived as

$$\begin{aligned} I_{\text{off},ij}(n) &= I_{M,ij}(n) - I_{M,ij,S} \\ (n) &= \frac{V_i[\varphi_j(n) - \varphi_j(n-1) - k_{ij}(\varphi_i(n) - \varphi_i(n-1))]}{2\pi f_S L_{ij} k_{ij}}. \end{aligned} \quad (7)$$

Then, for the MAB with N branches, the transient dc bias current of branch i can be derived by summarizing the current offsets of the $(N-1)$ different virtual DABs as (8), where V_j' is the dc voltage of branch j referred to the branch 1

$$\begin{aligned} I_{\text{off},i} &= \sum_{j\neq i}^{N} I_{\text{off},ij}(n) = \frac{1}{2\pi f_S}\sum_{j\neq i}^{N} \\ &\left(\frac{V_j'[\varphi_j(n) - \varphi_j(n-1) - k_{ij}(\varphi_i(n) - \varphi_i(n-1))]}{L_{ij}}\right). \end{aligned} \quad (8)$$

Fig. 5 shows the simulated voltage and current waveforms of a TAB converter during the transient process. The parameters are as: transformer turns ratio N_1: N_2: N_3 = 1: 1: 1, $L_1 = L_2 = L_3 = 160\ \mu$H, $L_m = 10$ mH, $r_{s1} = r_{s2} = r_{s3} = 0.05\ \Omega$, and $L_{s1} = L_{s2} = L_{s3} = 2\ \mu$H, where r_{s1}, r_{s2}, and r_{s3} are the equivalent resistors

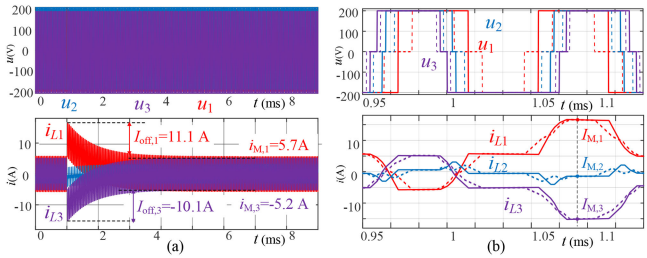

Fig. 5. Simulated waveforms of the TAB converter. (a) Overall waveforms. (b) Waveforms during transient process with different inner phase shift.

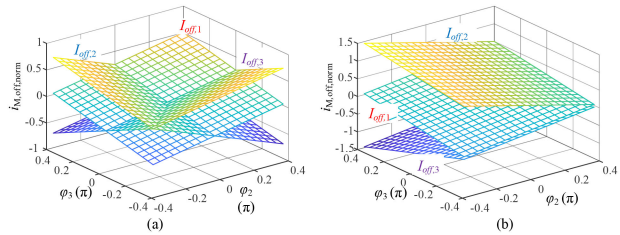

Fig. 6. Transient dc bias current of a TAB converter. (a) Case 1. (b) Case 2.

and L_{s1}, L_{s2}, and L_{s3} are the transformer leakage inductances. $V_1 = V_2 = V_3 = 200$ V and $f_S = 20$ kHz.

The phase-shift angles and inner phase-shift duties change from $\varphi_1 = 0$, $\varphi_2 = -0.2\ \pi$, and $\varphi_3 = -0.35\ \pi$ to $\varphi_1 = 0$, $\varphi_2 = 0.2\ \pi$, and $\varphi_3 = 0.35\ \pi$, as shown in Fig. 5(a). The inner phase-shift duties are as $d_1 = 0$, $d_2 = 0.05$, and $d_3 = 0.1$. The dc bias currents $I_{\text{off},1} = 11.1$ A and $I_{\text{off},3} = -10.1$ A meet well with the theoretical values $I_{\text{off},1,T} = 11.3$ A and $I_{\text{off},3,T} = -10.2$ A. Fig. 5(b) shows the detailed transient waveforms with two different sets of the inner phase-shift duties with $d_1 = 0$, $d_2 = 0.05$, and $d_3 = 0.1$ for the solid line waveforms and $d_1 = 0.4$, $d_2 = 0.3$, and $d_3 = 0.2$ for the dotted line waveforms. The middle currents are the same despite of the difference of the inner phase-shift duties.

Fig. 6 shows the normalized transient dc bias currents of the three branches in the TAB converter. The bias currents are relevant to both the initial and target phase-shift angles. Two cases with different initial phase-shift angels are considered: case 1 is $\varphi_1 = 0$, $\varphi_2 = 0$, and $\varphi_3 = 0$ and case 2 is $\varphi_1 = 0$, $\varphi_2 = -0.4\ \pi$, and $\varphi_3 = 0.4\ \pi$.

Assuming $\varphi_i(n) \in [-\varphi_{\max}, \varphi_{\max}]$, where $\varphi_{\max}$ is the maximum phase-shift angle of all the branches, then the maximum of the transient dc bias current is written as (9) shown at the bottom of the next page, which is twice the maximum middle current as (10) shown at the bottom of the next page.

Therefore, the transient dc bias model of the MAB is established by the analysis, and the derivation will be used in Section III.

III. Dynamic Modulation for DC Bias Current Elimination

In this section, a dynamic modulation method for transient dc bias current elimination will be proposed. The proposed

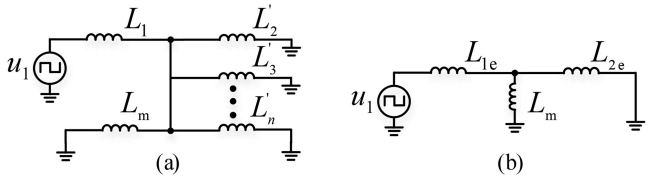

Fig. 7. Equivalent circuit. (a) Circuit with one source. (b) Simplified circuit.

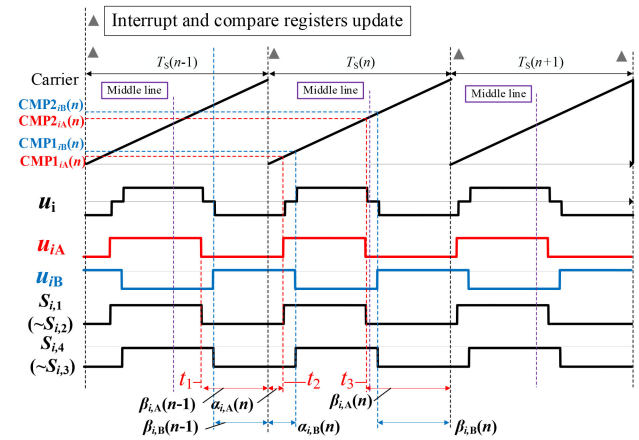

Fig. 8. Waveforms of the branch i with the transient modulation scheme.

dynamic modulation scheme is derived based on the two perspectives of the volt-second balance principle and instantaneous middle current bias elimination, respectively. Finally, the digital implementation of the proposed modulation method and its application will be presented.

A. Voltage-Second Balance

The equivalent circuit of the MAB considering one voltage source is shown in Fig. 7(a), which could be further simplified as Fig. 7(b). It is similar as the subcircuits of the DAB converter in [7] and [13]. The inductances are as $L_{1e} = L_1$, $L_{2e} = L_2'||L_3'\ldots||L_N'$. Making the voltage-second of each half-bridge or full-bridge in different branches balanced will be sufficient conditions for transient dc bias current elimination in both the windings and magnetizing inductance in MAB.

Taking the branch i as an illustration, as shown in Fig. 8, the voltage of the half-bridge A u_{iA} steps up from 0 to V_i at t_{ia} and steps down from V_i to 0 at t_{ic} and voltage of the right half-bridge u_{iB} steps down from V_i to 0 at t_{ib} and steps up from 0 to V_i at t_{id}. A sawtooth wave is utilized as the carrier. $S_{i,1}$, $S_{i,2}$, $S_{i,3}$, and $S_{i,4}$ are the gate signals for the four corresponding switches. The clock frequency of the counter for the carrier wave is f_C.

Considering the voltage-second balance for the half-bridge A of branch i between t_1 and t_3, as shown in Fig. 8, it can be obtained as

$$(\beta_{i,A}(n-1)+\alpha_{i,A}(n))V_i + (T_S-\alpha_{i,A}(n)-\beta_{i,A}(n))(-V_i)=0. \tag{11}$$

Then, $\alpha_{i,A}(n)$ is derived as

$$\begin{aligned}\alpha_{i,A}(n) &= (\alpha_{i,A,S}(n-1)+\alpha_{i,A,S}(n))/2,\\ \beta_{i,A}(n) &= \beta_{i,A,S}(n).\end{aligned} \tag{12}$$

The steady-state value of $\alpha_{i,A,S}(n)$ and $\beta_{i,A,S}(n)$ are written as

$$\begin{aligned}\alpha_{i,A,S}(n) &= (1-d_i(n))\frac{T_S}{4}+\frac{\varphi_i(n)}{2\pi}T_S,\\ \beta_{i,A,S}(n) &= (1+d_i(n))\frac{T_S}{4}-\frac{\varphi_i(n)}{2\pi}T_S.\end{aligned} \tag{13}$$

Thus, the rising duration in the nth cycle is derived as

$$\alpha_{i,A}(n) = \left[\left(1-\frac{d_i(n-1)+d_i(n)}{2}\right)\frac{1}{4}+\frac{1}{2\pi}\frac{\varphi_i(n-1)+\varphi_i(n)}{2}\right]T_S. \tag{14}$$

Similarly, $\alpha_{i,B}(n)$ is derived as

$$\alpha_{i,B}(n) = \left[\left(1+\frac{d_i(n-1)+d_i(n)}{2}\right)\frac{1}{4}+\frac{1}{2\pi}\frac{\varphi_i(n-1)+\varphi_i(n)}{2}\right]T_S. \tag{15}$$

B. Instantaneous Middle Current

The aforementioned derivation is based on the voltage-second balance principle between the same switching operations in two adjacent cycles. From the perspective of instantaneous winding current, a similar result can also be obtained. Combining (3) and (6), the transient dc bias current for the virtual DAB consisting of the branches i and j could be written as the sum of two terms $I_{\text{off},ij,i}$ and $I_{\text{off},ij,j}$ after algebraic manipulations as

$$\begin{cases} I_{\text{off},ij} = I_{\text{off},ij,i}+I_{\text{off},ij,j}\\ I_{\text{off},ij,i}\\ \quad = \frac{-V_i}{L_{ij}}\left[\alpha_{i,A}(n)+\alpha_{i,B}(n)-\frac{T_S}{2}\left(1+\frac{\varphi_i(n-1)+\varphi_i(n)}{2\pi}\right)\right]\\ I_{\text{off},ij,j}\\ \quad = \frac{V_i}{k_{ij}L_{ij}}\left[\alpha_{j,A}(n)+\alpha_{j,B}(n)-\frac{T_S}{2}\left(1+\frac{\varphi_j(n-1)+\varphi_j(n)}{2\pi}\right)\right]. \end{cases} \tag{16}$$

$$I_{\text{off},i,\max} = \frac{1}{2\pi f_S}\sum_{j\neq 1}^{N}\left(\frac{V_j'[\varphi_{\max}-(-\varphi_{\max})-k_{ij}(-\varphi_{\max}-(\varphi_{\max})]}{L_{ij}}\right) = 2I_{M,i,max} \tag{9}$$

$$I_{M,i} = \frac{1}{2\pi f_S}\sum_{j\neq i}^{N}\frac{V_j'(\varphi_j-k_{ij}\varphi_i)}{L_{ij}} \Rightarrow I_{M,i,\max} = \frac{1}{2\pi f_S}\sum_{j\neq i}^{N}\frac{V_j'(\varphi_{\max}+k_{ij}\varphi_{\max}))}{L_{ij}}. \tag{10}$$

Setting the two independent terms $I_{\text{off},ij,i}$ and $I_{\text{off},ij,j}$ equal to 0 will ensure $I_{\text{off},ij}=0$. Considering $I_{\text{off},ij,i}=0$, we could obtain

$$\alpha_{i,A}(n)+\alpha_{i,B}(n)=\frac{T_S}{2}\left(1+\frac{\varphi_i(n-1)+\varphi_i(n)}{2\pi}\right). \quad (17)$$

At steady state, the $\alpha_{i,A,S}(n-1)$ and $\alpha_{i,A,S}(n)$ meet the following:

$$\begin{aligned}&\alpha_{i,B,S}(n-1)-\alpha_{i,A,S}(n-1)\\&\quad=T_S d_i(n-1)/2,\quad \alpha_{i,B,S}(n)-\alpha_{i,A,S}(n)=T_S d_i(n)/2.\end{aligned} \quad (18)$$

For the mathematical symmetry, it is reasonable to set the transient values $\alpha_{i,A}(n)$ and $\alpha_{i,B}(n)$ to meet the following:

$$\alpha_{i,B}(n)-\alpha_{i,A}(n)=T_S(d_i(n-1)+d_i(n))/4. \quad (19)$$

To substitute (19) into (17), we could derive $\alpha_{i,A}(n)$ and $\alpha_{i,B}(n)$ with the same result as (14) and (15),which means that the derivation results from the perspectives of the voltage-second balance and the instantaneous current could be unified.

Thus, with the proposed dynamic modulation, the transient dc bias current of the arbitrary winding i in MAB could be eliminated to 0. The corresponding middle current reaches the steady-state value without transient dc bias as follows:

$$I_{M,i}(n)=I_{M,i,S}(n),\quad I_{\text{off},i}(n)=0. \quad (20)$$

It should be mentioned the initial phase-shift angle and inner phase-shift duty during the start process should be set to zero as

$$\varphi_i(0)=0,\quad d_i(0)=0. \quad (21)$$

C. Implementation and Application

For the digital implementation of the modulation, a sawtooth carrier is used to generate the PWM signals, as shown in Fig. 8. All the half bridges use the same carrier. When the compare values are equal to the counter value, actions will be triggered to change the corresponding gate signals. The $\text{CMP1}_{iA}(n)$ and $\text{CMP2}_{iA}(n)$ are the corresponding compare registers to generate the signals of half-bridge A in the nth cycle, the $\text{CMP1}_{iB}(n)$ and $\text{CMP2}_{iB}(n)$ are the corresponding compare registers for half-bridge B. With the proposed dynamic modulation, the four compare values in the nth can be calculated as follows:

$$\begin{cases}\text{CMP1}_{iA}(n)\\=\left[\left(1-\frac{d_i(n-1)+d_i(n)}{2}\right)\frac{1}{4}+\frac{1}{2\pi}\frac{\varphi_i(n-1)+\varphi_i(n)}{2}\right]T_S f_C\\ \text{CMP2}_{iA}(n)=\left[(3-d_i(n))\frac{1}{4}+\frac{\varphi_i(n)}{2}\right]T_S f_C\\ \text{CMP1}_{iB}(n)\\=\left[\left(1+\frac{d_i(n-1)+d_i(n)}{2}\right)\frac{1}{4}+\frac{1}{2\pi}\frac{\varphi_i(n-1)+\varphi_i(n)}{2}\right]T_S f_C\\ \text{CMP2}_{iB}(n)=\left[(3+d_i(n))\frac{1}{4}+\frac{\varphi_i(n)}{2}\right]T_S f_C.\end{cases} \quad (22)$$

The four compare values are updated once at the start of each cycle, as shown in Fig. 8. The switching and update frequency is fixed, which is the same as the carrier frequency.

Fig. 9 shows the simulated waveforms of an MMAB converter with four branches, as shown in Fig. 3(b), during the transient process, including startup and normal modes. Four transformers with the same parameters are used. The system parameters are as follows: N_1: N_2 = 1: 1, $r_{s1}=r_{s2}=0.05\ \Omega$, $L_{s1}=L_{s2}=2\ \mu$H, and $L_m=12$ mH for the transformer. $L_1=L_2=L_3=L_4=160\ \mu$H, $V_1=V_2=V_3=V_4=300$ V, and $f_S=20$ kHz. The converter starts up at 50 μs with $\varphi_1=0$, $d_1=0$, $\varphi_2=-0.1\ \pi$, $d_2=0$, $\varphi_3=0.05\ \pi$, $d_3=0$, $\varphi_4=0.1\ \pi$, and $d_4=0$. The corresponding power is $P_1=166$ W, $P_2=1315$ W, $P_3=-440$ W, and $P_4=-1030$ W. Then, the power changes to $P_1=790$ W, $P_2=2230$ W, $P_3=-2030$ W, and $P_4=-927$ W at 150 μs with $\varphi_1=0$, $d_1=0$, $\varphi_2=-0.2\ \pi$, $d_2=0.1$, $\varphi_3=0.35\ \pi$, $d_3=0.1$, $\varphi_4=0.2\ \pi$, and $d_4=0.1$. At 250 μs, the power changes to $P_1=166$ W, $P_2=1315$ W, $P_3=-440$ W, and $P_4=-1030$ W with $\varphi_1=0$, $d_1=0$, $\varphi_2=-0.1\ \pi$, $d_2=0$, $\varphi_3=0.05\ \pi$, $d_3=0$, $\varphi_4=0.1\ \pi$, and $d_4=0$. During the transient process, the modulation method switches between SPS and GPS modulations' schemes. No transient dc bias exists for both the startup and normal modes.

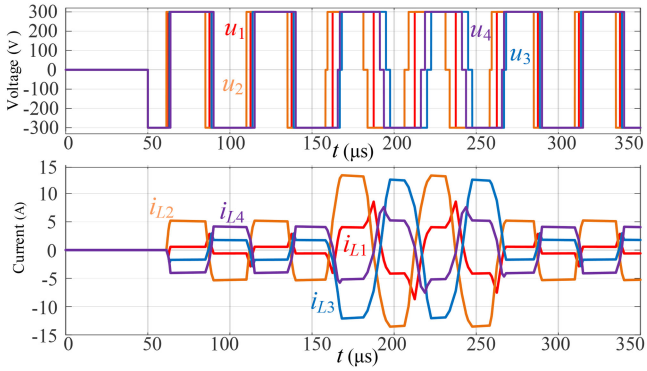

Fig. 9. Simulated waveforms of MMAB during the startup and normal processes.

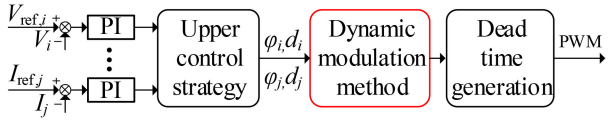

Fig. 10. Closed-loop control based on the dynamic modulation method.

Fig. 10 shows the closed-loop control scheme based on the dynamic modulation method, assuming that the dc voltage of the port i V_i and the dc current of port j I_j need to be regulated, respectively. The dynamic modulation generates the PWM signals according to the phase angles and inner phase-shift duties, which are calculated by the upper control strategy, i.e., power decoupling, current stress, and losses optimization. Thus, the proposed dynamic modulation method is compatible and complementary with the existing control strategies and optimized modulations for steady-state performance.

IV. Experimental Validation

A TAB converter and an MMAB converter with the same parameters as in the simulation in Sections II and III are set up to verify the proposed dynamic modulation method. The

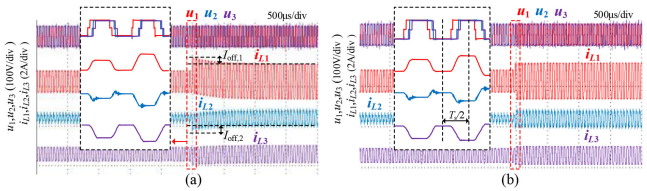

Fig. 11. Experimental waveforms of TAB with phase-shift angles and duty cycles change using a GPS modulation scheme. (a) With a direct transition. (b) With the proposed dynamic modulation method.

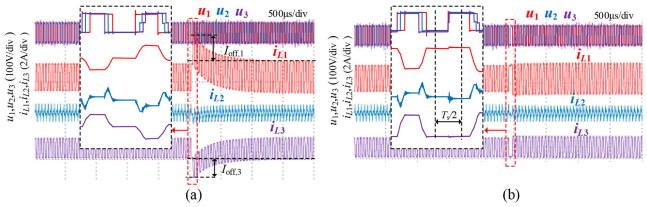

Fig. 12. Experimental waveforms of TAB with the phase-shift angles and modulation change (from SPS to GPS modulation). (a) With a direct transition. (b) With the proposed dynamic modulation method.

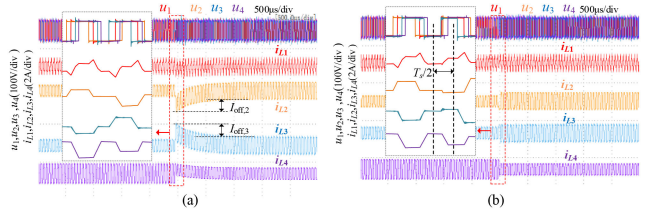

Fig. 13. Experimental waveforms of MMAB with phase-shift angles change using SPS modulation. (a) With a direct transition. (b) With the proposed dynamic modulation method.

dynamic modulation is compared with the conventional modulation, which is a direct transition in different transient conditions. The deadtime 1 μs is used in the experiments.

Fig. 11 shows the waveforms of the TAB converter using GPS modulation scheme. The dc voltages are 100 V. The phase-shift angles and the inner phase-shift duties change from $\varphi_1 = 0$, $d_1 = 0.1$, $\varphi_2 = 0.2\ \pi$, $d_2 = 0.05$, $\varphi_3 = 0.25\ \pi$, and $d_3 = 0.1$ to $\varphi_1 = 0$, $d_1 = 0.05$, $\varphi_2 = 0.2\ \pi$, $d_2 = 0.1$, $\varphi_3 = 0.35\ \pi$, and $d_3 = 0.1$ with the corresponding power changes from $P_1 = 175$ W, $P_2 = -57$ W, and $P_3 = -115$ W to $P_1 = 197$ W, $P_2 = -17$ W, and $P_3 = -176$ W. Both the phase-shift angels and the inner phase-shift duties change. The transient dc bias currents $I_{\text{off},1}$ and $I_{\text{off},2}$ are mitigated after the dynamic modulation is utilized.

Fig. 12 shows the waveforms of the TAB converter that switches from the SPS modulation to GPS modulation. The control parameters change from $\varphi_1 = 0$, $d_1 = 0$, $\varphi_2 = -0.2\ \pi$, $d_2 = 0$, $\varphi_3 = -0.35\ \pi$, and $d_3 = 0$ to $\varphi_1 = 0$, $d_1 = 0$, $\varphi_2 = 0.2\ \pi$, $d_2 = 0.1$, $\varphi_3 = 0.35\ \pi$, and $d_3 = 0.1$ with the corresponding power changes from $P_1 = -198$ W, $P_2 = 18$ W, and $P_3 = 183$ W to $P_1 = 198$ W, $P_2 = -17$ W, and $P_3 = -177$ W. With the proposed method, the transient dc bias currents are eliminated even when the modulation method changes and power flow reverses simultaneously.

Fig. 13 shows the waveforms of the MMAB converter using the SPS modulation. The dc voltages are 100 V. The phase-shift angles change from $\varphi_1 = 0$, $\varphi_2 = -0.2\ \pi$, $\varphi_3 = 0.2\ \pi$, and $\varphi_4 = 0.35\ \pi$ to $\varphi_1 = 0$, $\varphi_2 = 0.3\ \pi$, $\varphi_3 = -0.3\ \pi$, and $\varphi_4 = 0.2\ \pi$. The corresponding power changes from $P_1 = 89$ W, $P_2 = 254$ W, $P_3 = -104$ W, and $P_4 = -230$ W to $P_1 = 63$ W, $P_2 = -205$ W, $P_3 = 273$ W, and $P_4 = -122$ W. The transient dc bias currents are mitigated for the dynamic modulation method.

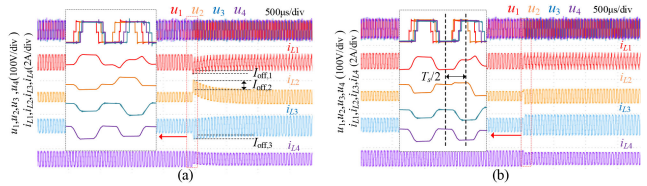

Fig. 14. Experimental waveforms of MMAB with phase-shift angles and duty cycles change using a GPS modulation scheme. (a) With a direct transition. (b) With the proposed dynamic modulation method.

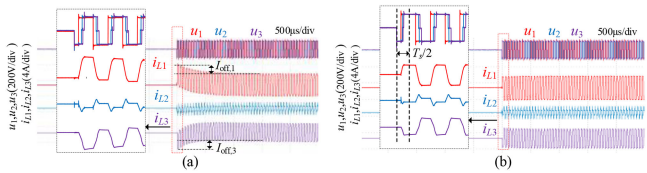

Fig. 15. Experimental waveforms of TAB during the startup process. (a) With a direct transition. (b) With the proposed dynamic modulation method.

Fig. 14 shows the waveforms of the MMAB converter. The dc voltages are 100 V. For generality, both the phase-shift angle and the inner phase-shift duty change from $\varphi_1 = 0$, $d_1 = 0.1$, $\varphi_2 = 0.2\ \pi$, $d_2 = 0.05$, $\varphi_3 = 0.25\ \pi$, $d_3 = 0.1$, $\varphi_4 = 0.3\ \pi$, and $d_4 = 0.1$ to $\varphi_1 = 0$, $d_1 = 0.05$, $\varphi_2 = -0.3\ \pi$, $d_2 = 0.1$, $\varphi_3 = 0.35\ \pi$, $d_3 = 0.1$, $\varphi_4 = 0.2\ \pi$, and $d_4 = 0.1$. The corresponding power changes from $P_1 = 210$ W, $P_2 = -9$ W, $P_3 = -70$ W, and $P_4 = -126$ W to $P_1 = 68$ W, $P_2 = 264$ W, $P_3 = -217$ W, and $P_4 = -106$ W. The transient dc bias currents are eliminated for the dynamic modulation method.

Fig. 15 shows the waveforms of the TAB converter during the startup process. The phase-shift angles and the inner phase-shift duties change from the initial state to $\varphi_1 = 0$, $d_1 = 0$, $\varphi_2 = 0.2\ \pi$, $d_2 = 0.05$, $\varphi_3 = 0.3\ \pi$, and $d_3 = 0.1$ with the corresponding powers $P_1 = 190$ W, $P_2 = -36$ W, and $P_3 = -150$ W. The currents reach the new steady-state values within half cycle without the transient dc bias with the proposed method.

The above waveforms show that the transformer currents reach to the new steady state within half cycle $T_S/2$ with the proposed dynamic modulation method, which is independent of the modulations, operation modes, and power flow directions.

V. Conclusion

This letter proposes the general transient dc bias current model for MAB, which is irrespective of the power directions and modulation methods. The theoretical derivation and simulation results reveal that the transient dc bias is only related to the phase-shift angles and independent on the inner phase shift. On top of that, a universal dynamic modulation method is proposed for transient dc bias mitigation with the fixed switching

frequency, which is irrespective of the modulations and valid for both the normal and startup modes. With the proposed dynamic modulation method, the superior performance with transient dc bias mitigation within a half cycle is achieved in various operation modes and transient conditions, which is validated by the experimental results of a TAB and MMAB converter, respectively. The dynamic modulation method, along with the derivation process, could also be applicable to the DAB and MMAB converters.

REFERENCES

[1] S. Bandyopadhyay, P. Purgat, Z. Qin, and P. Bauer, "A multiactive bridge converter with inherently decoupled power flows," *IEEE Trans. Power Electron.*, vol. 36, no. 2, pp. 2231–2245, Feb. 2021.

[2] T. Pereira, F. Hoffmann, R. Zhu, and M. Liserre, "A comprehensive assessment of multiwinding transformer-based DC–DC converters," *IEEE Trans. Power Electron.*, vol. 36, no. 9, pp. 10020–10036, Sep. 2021.

[3] Y. Chen, P. Wang, H. Li, and M. Chen, "Power flow control in multi-active-bridge converters: Theories and applications," in *Proc. IEEE Appl. Power Electron. Conf. Expo.*, 2019, vol. 2, pp. 1500–1507.

[4] C. Gu, Z. Zheng, L. Xu, K. Wang, and Y. Li, "Modeling and control of a multiport power electronic transformer (PET) for electric traction applications," *IEEE Trans. Power Electron.*, vol. 31, no. 2, pp. 915–927, Feb. 2016.

[5] N. Hou and Y. W. Li, "Overview and comparison of modulation and control strategies for a nonresonant single-phase dual-active-bridge dc-dc converter," *IEEE Trans. Power Electron.*, vol. 35, no. 3, pp. 3148–3172, Mar. 2020.

[6] B. Zhao, Q. Song, W. Liu, and Y. Zhao, "Transient dc bias and current impact effects of high-frequency-isolated bidirectional dc–dc converter in practice," *IEEE Trans. Power Electron.*, vol. 31, no. 4, pp. 3203–3216, Apr. 2016.

[7] K. Takagi and H. Fujita, "Dynamic control and performance of a dual-active-bridge dc–dc converter," *IEEE Trans. Power Electron.*, vol. 33, no. 9, pp. 7858–7866, Sep. 2018.

[8] R. Chattopadhyay, U. Raheja, G. Gohil, V. Nair, and S. Bhattacharya, "Sensorless phase shift control for phase shifted dc-dc converters for eliminating dc transients from transformer winding currents," in *Proc. IEEE Appl. Power Electron. Conf. Expo.*, 2018, pp. 1882–1889.

[9] X. Li and Y.-F. Li, "An optimized phase-shift modulation for fast transient response in a dual-active-bridge converter," *IEEE Trans. Power Electron.*, vol. 29, no. 6, pp. 2661–2665, Jun. 2014.

[10] J. Hu, S. Cui, S. Wang, and R. W. De Doncker, "Instantaneous flux and current control for a three-phase dual-active bridge DC–DC converter," *IEEE Trans. Power Electron.*, vol. 35, no. 2, pp. 2184–2195, Feb. 2020.

[11] S. Dutta, S. Hazra, and S. Bhattacharya, "A digital predictive current-mode controller for a single-phase high-frequency transformer-isolated dual-active bridge dc-to-dc converter," *IEEE Trans. Ind. Electron.*, vol. 63, no. 9, pp. 5943–5952, Sep. 2016.

[12] S. Wei, Z. Zhao, K. Li, L. Yuan, and W. Wen, "Deadbeat current controller for bidirectional dual-active-bridge converter using an enhanced SPS modulation method," *IEEE Trans. Power Electron.*, vol. 36, no. 2, pp. 1274–1279, Feb. 2021.

[13] J. Hu, S. Cui, D. von den Hoff, and R. W. De Doncker, "Generic dynamic phase-shift control for bidirectional dual-active bridge converters," *IEEE Trans. Power Electron.*, vol. 36, no. 6, pp. 6197–6202, Jun. 2021.

[14] S. Mu, Z. Guo, and Y. Luo, "Universal modulation scheme to suppress transient DC bias current in dual active bridge converters," *IEEE Trans. Power Electron.*, vol. 37, no. 2, pp. 1322–1333, Feb. 2022.

[15] P. Zumel, C. Fernandez, A. Lazaro, M. Sanz, and A. Barrado, "Overall analysis of a modular multi active bridge converter," in *Proc. IEEE 15th Workshop Control Model. Power Electron.*, Santander, Spain, 2014, pp. 1–9.

[16] L. Ortega, P. Zumel, C. Fernández, J. López-López, and A. Lázaro, "Power distribution algorithm and steady-state operation analysis of a modular multiactive bridge converter," *IEEE Trans. Transp. Electrific.*, vol. 6, no. 3, pp. 1035–1050, Sep. 2020.

[17] K. Li *et al.*, "Design and implementation of four-port megawatt-level high-frequency-bus based power electronic transformer," *IEEE Trans. Power Electron.*, vol. 36, no. 6, pp. 6429–6442, Jun. 2021.

[18] W. Wen, K. Li, Z. Zhao, L. Yuan, X. Mo, and W. Cai, "Analysis and control of a four-port megawatt-level high-frequency-bus-based power electronic transformer," *IEEE Trans. Power Electron.*, vol. 36, no. 11, pp. 13080–13095, Nov. 2021.